Yttrium doped ZnO nanorod arrays for increased charge mobility and carrier density for enhanced solar water splitting

Article (Accepted Version)

Yttrium Doped ZnO Nanorod Arrays for Increased Charge Mobility and Carrier Density for Enhanced Solar Water Splitting

Daniel Commandeur, Grant Brown, Peter McNulty, Christopher Dadswell, John Spencer, Qiao Chen*

Department of Chemistry, School of Life Sciences, University of Sussex, Brighton, BN1 9RH, UK

*Corresponding Author

Abstract

An innovative procedure is presented, when for the first time, yttrium doped ZnO vertically aligned nanorods have been synthesized using a unique rapid microwave assisted method. In comparison with pristine ZnO NRs, the Y-doped samples present more favourable morphology along with reduced crystallinity due to substitutional defects, Y_{Zn}. The Y acted as a shallow donor type defect, leading to an 80% increase in dopant density, to 1.36×10^{18} cm^{-2} in the 0.15% Y sample. The transmission line model was used to analyse the transport properties. It was found that a 1000-fold increase in conductivity and electron mobility was achieved by doping 0.15% Y, resulting in a high density of donors which fill charge traps. Meanwhile, a significant improvement in conductivity was accompanied by greater electron hole recombination and band gap reduction. Analysis of photoluminescence spectra reveals the effect of Y doping on native point defects, initially reducing Zn^{2+} vacancies by filling with Y_{Zn}, followed by the reduction of O^{2-} vacancies with interstitial doping at higher Y concentration. With a fine balance of superior conductivity and charge recombination rate, the photocatalytic water splitting performance was optimised achieving photocurrent of 0.84 mA cm^{-2} at 1.23 V_{RHE} with 0.1% Y doping. This corresponded to a 47% enhancement in photoconversion efficiency compared to the pristine sample.

1 Introduction

In order to meet the challenge of the energy crisis, the 'hydrogen economy' has the potential to play a significant role in the storage and renewable generation of energy.[1] Photoelectrochemical (PEC) water splitting is an emerging method of hydrogen production that has seen great advances since its first demonstration by Fujishima and Honda.[2–4] In this rapidly advancing field various materials have been applied, such as highly oriented rutile TiO_2 nanorods,[5] along with flexible polymeric carbon nitride films.[6] Stability in water, wide electronic band gap and appropriate band edge position afford ZnO suitable properties for this process,[7] furthermore, high electron mobility and high charge carrier density give this material an advantage over TiO_2.[8] Nanostructured photoanodes provide increased photoconversion efficiency (PCE) in systems reliant on Faradaic charge transfer,[9] leading to a plethora of ZnO morphologies such as nanoparticles,[10] nanotubes,[11] nanoflowers and nanorods.[12,13] The electronic and optical properties of ZnO can be improved by extrinsic doping, allowing further light absorption in the visible spectrum through band gap narrowing,[14] or increased conductivity. By introducing shallow donors, electron concentration can be raised, resulting in the reduction of transport resistance and increasing the rate of photolysis.[15]

In this work, yttrium doped ZnO nanorods (NRs) have been applied to PEC water splitting for the first time, for a significant enhancement in PCE. Vertically aligned ZnO NRs were grown via rapid microwave assisted synthesis, with Y addition in the growth solution leading to reduced crystallinity and more favourable geometry. This also resulted in greater n-type doping along with dramatically increased electron mobility, improving the charge dynamics in the semiconductor bulk. This led to a significant increase in photocurrent density and

therefore water splitting ability, when compared to the pristine sample, with potential application to photovoltaic technology in future.

Yttrium doped ZnO is well known for its conductivity in the strongly n-type semiconductor,[16–20] leading to applications as a transparent conducting oxide,[21,22] gas ionization and humidity sensor.[23,24] Favourable optical properties of Y doped ZnO have led to applications as a photoanode in organic light emitting diodes,[25] displaying enhanced UV emission.[26] These attractive prospects have led to the exploration of Y doped ZnO powder as a photocatalyst for dye degradation,[27,28] and for hydrogen generation in the water-lactic acid system.[29] Y doped ZnO NRs were applied to solar water splitting coated with carbon nitride achieving a photocurrent of 0.4 mA cm^{-2} at 1.23 V_{RHE}.[30] In all cases, the Y doping led to a remarkable improvement in catalytic rates.

This study aimed to better understand and quantify the effects of Y doping on the charge transport and interfacial transfer in the ZnO NR/electrolyte system. Therefore, electrochemical impedance spectroscopy (EIS) was performed and analyzed with the transmission line model, determining electron mobility, conductivity, recombination resistance and chemical capacitance. This method has been applied to many nanocrystalline systems including mesoporous TiO_2,[31] mesoporous Fe_2O_3 and organic heterojunction films.[32,33] Furthermore, it has become a common characterisation technique in dye sensitised and perovskite solar cells,[34–37] as well as ZnO nanotube and nanorod arrays.[11,38] Here, we used the transmission line model, for the first time, to analyse the effects of Y doping on ZnO, revealing dramatically improved electron mobility.

In this paper yttrium doping is presented to be an effective method of increasing the efficiency of ZnO NR water splitting photoanodes. Incorporation of Y into the ZnO lattice led to reduced crystallinity and improved morphology by reducing the NR diameter from 111 to 92 nm at 0.15% Y doping. The extrinsic atomic addition was confirmed as a shallow donor, increasing n-type doping by 80%, which also led to a significant enhancement in trap limited electron mobility reflected by several orders of magnitude gain in conductivity. Such an improvement would not be possible without the effect of Y on the native point defects of ZnO, where photoluminescence (PL) spectroscopy displayed a reduction in both V_O and V_{Zn} densities, lowering electron scattering through the bulk. Furthermore, UV-Vis spectroscopy revealed the reduction in band gap of the doped ZnO, allowing greater visible light absorption. However, further increasing the doping level also led to faster electron hole recombination and therefore energy loss. Ultimately yttrium content was optimised at 0.1% leading to a 47% enhancement in photoconversion efficiency.

2 Experimental Method

2.1 Synthesis of Nanorods

All chemicals used were purchased from Sigma Aldrich with no further purification. Transparent conducting glass substrates (fluorine-doped tin oxide FTO) were cleaned by sonication in acetone, isopropanol and deionised (DI) water for 15 minutes in each solvent. Each 12 × 20 mm FTO glass was seeded using a 0.1 M zinc acetate solution in DI water with added 0.6 wt% polyvinyl alcohol for added viscosity. The solution was spin coated using a two stage program, 800 RPM for 90 seconds followed by 30 seconds at 2000 RPM in order to

remove beads of solution from the edge. This was followed by annealing in air at 500°C for 20 minutes in order to form the zinc oxide seeding layer.[39]

The vertically aligned NRs were synthesised using a microwave chemical bath deposition. The details were published separately.[40] Each cycle was heated at 100 W to 100°C for a 30 minute holding time. A total of 4 cycles were used for each ZnO sample, substrates were placed face down in 20 ml aqueous solution of 40 mM zinc nitrate and hexamethylenetetramine (HMT) in 1:1 molar ratio. Cycles took 3 minutes to reach temperature and 5 minutes to cool, the microwave reactor used was the CEM Discover.

Samples were subsequently annealed in air at 500°C for 30 minutes. Yttrium doped samples were produced by 0.5, 1, and 2% molar addition of yttrium nitrate (with respect to zinc nitrate) to the growth solution.

2.2 Materials Characterisation

The real concentration of yttrium dopants was measured by inductively coupled plasma mass spectrometry (ICP-MS, Agilent 7500ce). Samples were prepared for ICP-MS by dissolving in 2 ml, 1.5 wt% nitric acid, followed by dilution to 50 ml volume by DI water addition. Scanning electron microscopy (SEM, JSM820 M, Jeol) was used to analyse the morphology of the samples. The crystallinity and structure orientation of the nanostructures were analysed by powder x-ray diffractometer (XRD, Siemens D500). The dimensions of the nanorods were measured from SEM images using Image J software (National Institutes of Health, USA). A standard 3-electrode set up, with Ag/AgCl reference and platinum counter electrodes was used for both water splitting photocurrent and electrical impedance spectroscopy (EIS). ZnO NR

arrays were grown on FTO-glass substrate (Sigma-Aldrich UK) forming the photoanode. Using a 0.5 M Na_2SO_4 electrolyte and a linear potential scan from 0.2 to 1.6 V_{RHE} photocurrents were determined. A solar simulator (Oriel LCS-100, Newport) with an AM 1.5 G filter at a distance calibrated to 100 $mWcm^{-2}$ was used as the light source. PL spectra were characterised using a fluorescence spectrometer (Perkin Elmer LS 45) and UV-Vis diffuse reflectance spectra used to determine optical band gap were acquired using Ocean Optics ISP-REF integrating sphere equipped with an inbuilt tungsten-halogen illumination source 300 nm $\leq \lambda \leq$ 1000 nm, with MgO reference. EIS was performed in the dark using a Palm Sens 3 (PalmSens BV) electrochemical sensor, processed using PS Trace 4.8 (PalmSens BV) and Elchemea Analytical (DTU Energy, Technical University of Denmark).

3 Results and Discussion

3.1 Morphology and Crystallinity

High surface area and fast charge transport are beneficial to the rate of water photolysis.[41,42] The presence of dopant ions in the growth solution often affects the morphology and crystallinity of zinc oxide NRs, due to the surface charging of the wurtzite structure in a basic solution.[14] Y^{3+} ions have been previously reported to form a negatively charged complex, stifling the lateral growth of ZnO due to the partial positive charge of the NR walls.[23] The effect of Y doping on the morphology was observed by SEM, shown in Fig. 1. Cross sectional SEM used to measure NR length and diameter distributions can be found in Fig. S1. The averaged ZnO NRs diameters and lengths are plotted in as shown in Fig. S2.

With increase in Y concentration, the diameter of ZnO NRs decreases from 111 to 92 nm. This effect is also conversely seen in the length of the nanowires, from 1650 to > 2000 nm. This is due to the opposed charging of the top 002 face, leading to increased growth in the c axis. This could be beneficial to PEC performance as larger aspect ratios lead to greater interfacial area for charge transfer.

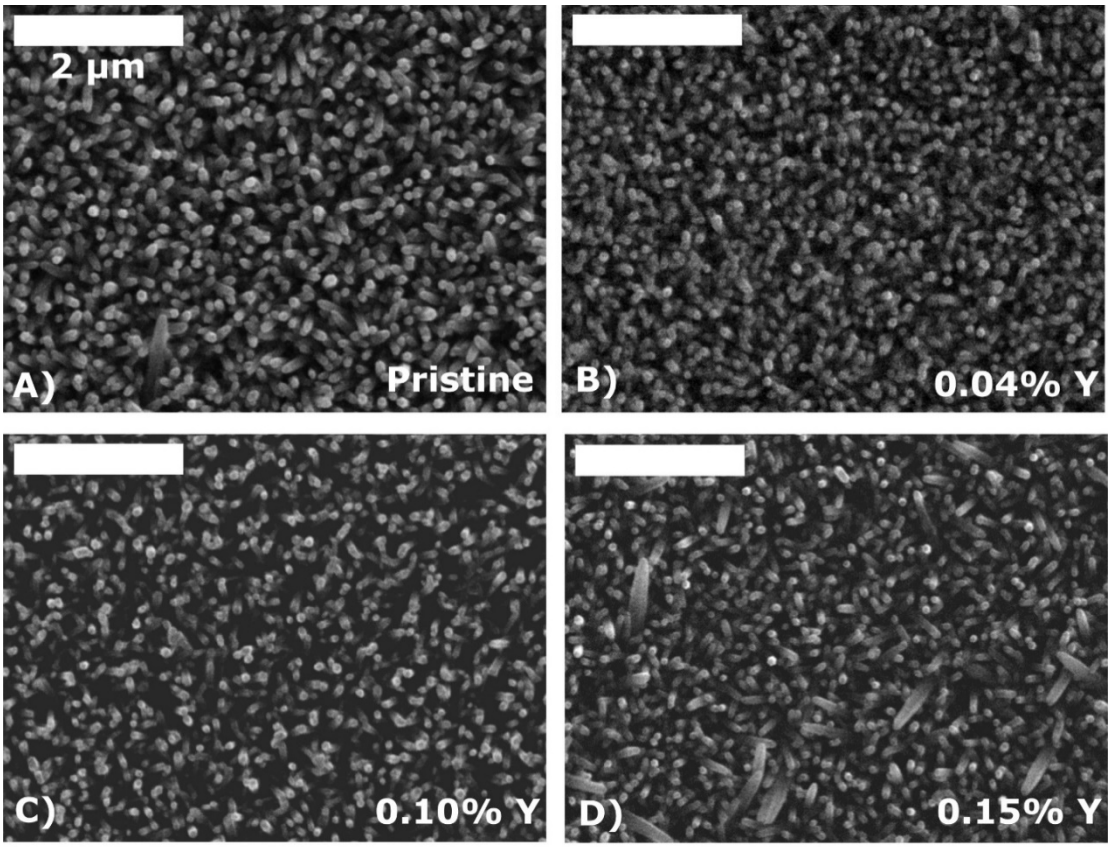

Figure 1: SEM images A), B), C) and D) corresponding to Y molar doping of 0, 0.04%, 0.10% and 0.15% respectively. The scale bars correspond to 2 µm.

ICP-MS was used to give accurate concentrations of Y. To assess the averaged dopant concentration, the ZnO NRs were dissolved in acid first. With growth solutions containing 0,

0.5, 1 and 2% molar addition of yttrium nitrate, dopant concentrations of 0, 0.04, 0.10 and 0.15% of Y were achieved in the ZnO NRs.

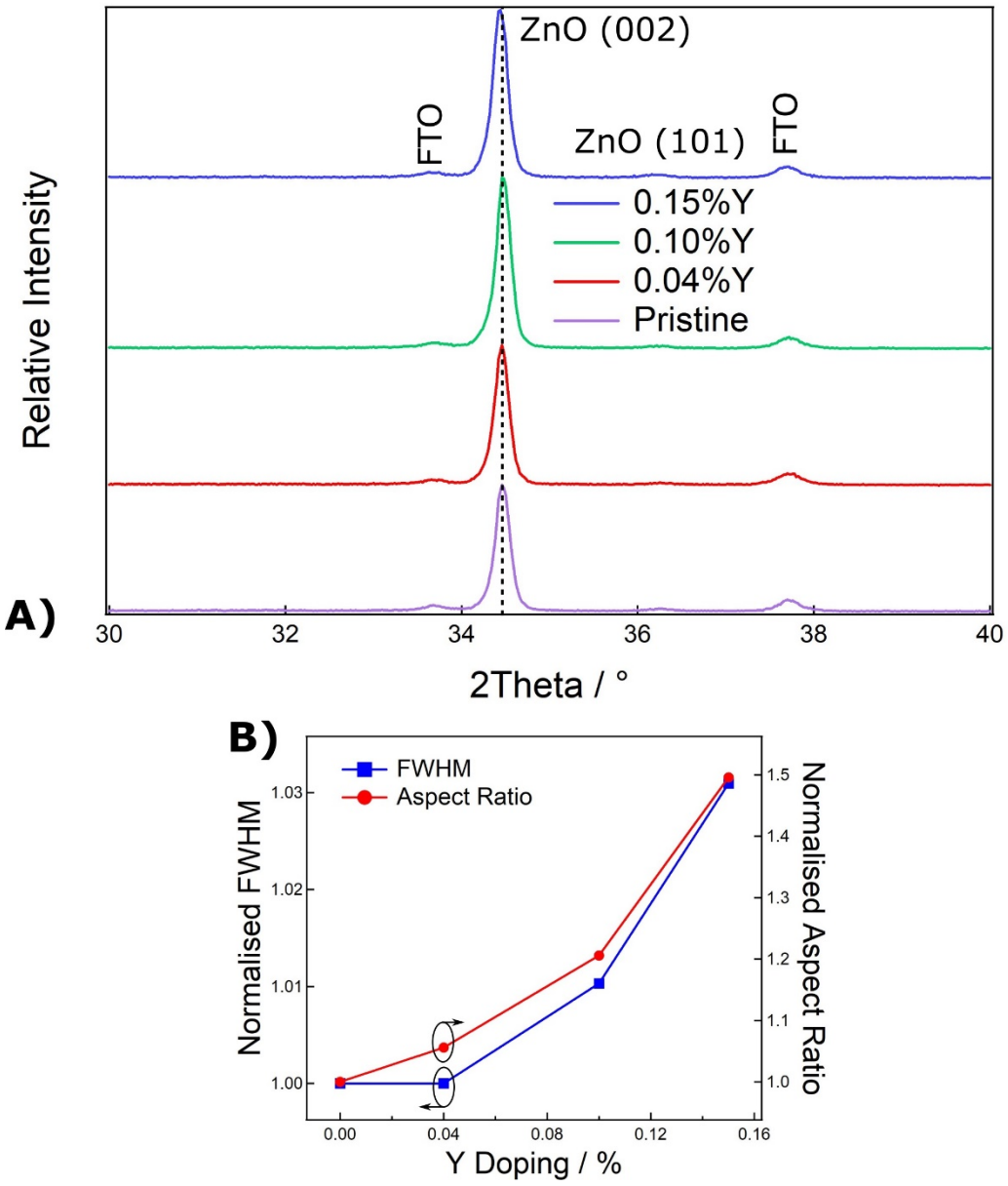

Figure 2: A) A segment of wide scan XRD of the different samples. B) The normalised FWHM compared to the normalised NW aspect ratio as a function of dopant concentrations.

Powder XRD was used to analyse the crystal properties of the samples, shown in Fig. 2A. Both the wurtzite ZnO (JCPDS 36-1451) and FTO (JCPDS 71-0652) structures were identified. No new peaks were observed from the presence of yttrium oxide due to low abundance and homogenous incorporation into the zinc oxide. This is consistent with literature.[23,43] The feature dominating the spectra is the c-axis ZnO (002) peak at 34.5°. This is typical of NR arrays due to the strong vertical alignment of the structures, which has the (002) plane parallel to the substrate. The other ZnO signals were dwarfed in comparison due to this unique crystal alignment.

Values of peak position and full width half maximum (FWHM) provide information about the lattice spacing and crystal domain size respectively. The most significant trend from increased doping is seen in the FWHM increase for the (002) peak, seen in Fig. 2B with the expanded (002) peak shown in Fig. S3. This corresponds to a reduction in crystallinity due to the Y ions incorporated into the ZnO lattice, along with a decrease in grain size *D* given by the Debye-Scherrer formula.[44]

$$D = \frac{0.9\lambda}{\beta \cos\theta_{hkl}} \quad (1)$$

Where λ is the x-ray wavelength, β and θ are the FWHM and the angle of diffraction, respectively. The crystal grain size decreases from 42.8 nm (0% Y) to 41.6 nm (0.15% Y) due to the lattice addition. This trend closely follows the aspect ratio change with yttrium doping, confirming the linked morphological and crystallographic effects. A reduction in diffraction angle is seen for 0.15% doping due to the larger ionic radius of Y^{3+}, 0.92Å, compared to Zn^{2+}, 0.74Å.[45] This stretches the crystal wurtzite structure leading to a larger lattice constant, from

5.201 to 5.204 Å from pristine to 0.15% Y respectively. As the dopant concentration increases, the diffraction peak width increases as well as the peak height, Fig. 2A. Hence, the overall diffraction intensity from the (002) increases. Such increase can be explained by the longer NWs in the c axis, leading to greater abundance of (002) crystal plane.

3.2 Optical and Electronic Properties

Electrical Impedance Spectroscopy (EIS) is a powerful tool for understanding charge transfer the semiconductor-electrolyte systems. The Mott-Schottky plot of $1/C^2$ vs potential bias yields the valuable parameters of dopant density N_D, and flatband potential V_{FB}.[46] Both values are generally determined by the gradient and extrapolated intercept of the linear region. However, Mora-Seró *et al.* developed a more accurate model reflecting the ZnO NR cylindrical geometry.[47] The depletion region in an array of vertically aligned NRs was calculated by solving the Poisson equation using cylindrical polar coordinates. With this geometry correction, the potential bias, V, is related to the capacitance per unit area, C_s, following Eq. 2.

$$V - V_{FB} = -\frac{N_D e}{4\epsilon}\left[R^2 - \frac{C_s R^3}{2\epsilon + C_s R} + R^2 \ln \frac{C_s R}{2\epsilon + C_s R}\right] \quad (2)$$

Where e is the electron charge; ϵ is the product of the permittivity of free space and dielectric constant of ZnO, valued at 10. R is the NR radius in cm as measured by SEM. The derivation of Eq. 2 along with the calculation of C_s from raw values of C can be found in the supplementary information (section S1.1). Eq. 2 is significantly different from the planar Mott-Schottky model in which the $1/C^2$ is linearly proportional to $V\text{-}V_{FB}$, and inversely proportional to the donor density. The experimental data (points) and model fits (lines) are

shown in Fig. 3A. Despite some divergence seen at higher potentials, the fit is accurate over a far greater potential window than the typical linear model. This implies the cylindrical morphology has significant effects on the impedance properties of the NR material and the non-planar model could improve the accuracy of N_D and V_{FB} in comparison to the typical Mott-Schottky analysis for planar electrodes.

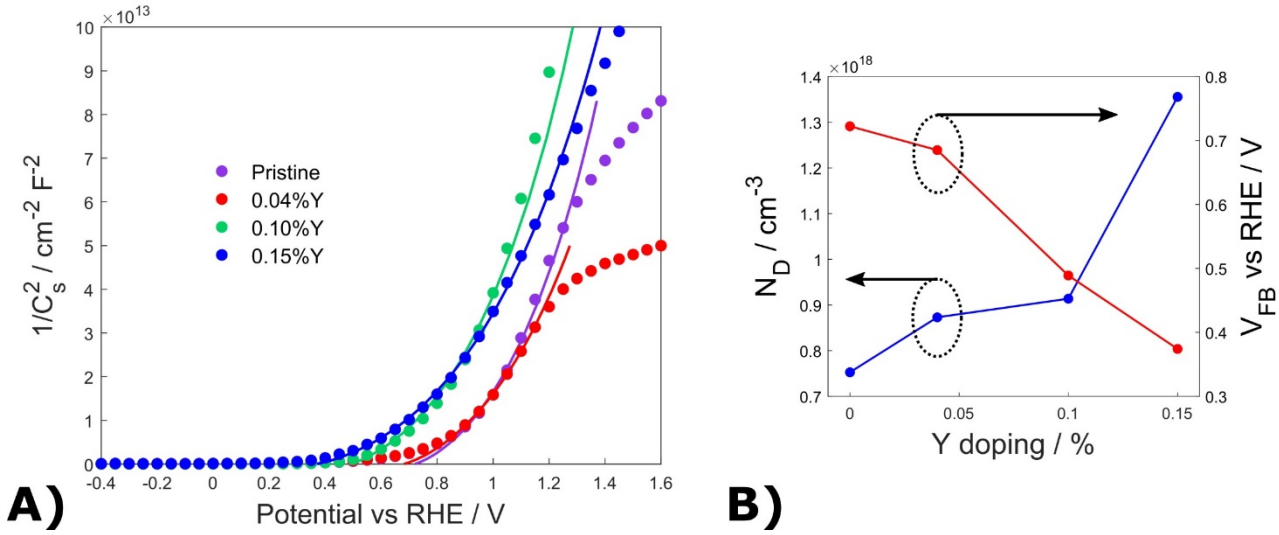

Figure 3: A) Sample capacitance, $1/C_s^2$ vs potential bias, dots denote experimentally measured data and lines show simulated model fits. B) N_D and V_{FB} against doping.

As expected, increased doping leads to a higher dopant density in the NR samples, due to Y^{3+} ions acting as shallow n-type donors to the conduction band.[17] This leads to lower transport resistance and higher conductivity, suitable for rapid charge collection.[48] Fig. 3B shows the obtained N_D and V_{FB} values as a function of doping level. The value of N_D monotonically increases from 7.53×10^{17} cm^{-3} for pristine, to 1.36×10^{18} cm^{-3} of 0.15% doping. At low level doping, the modest increase in N_D is possibly due to reduction in oxygen

vacancies, V_O and Fermi level pinning within the conduction band.[49] However, high level doping fills more states in the band, leading to a higher energy Fermi level which in turn, increases the formation energy of n-type native defects such as V_O.[50] This is confirmed by the negative shift in flat band potential with increasing Y doping. This effect was also observed by Kelley *et al.*, using low levels of yttrium doping in CdO films.[51]

In order to investigate the fundamental material properties of conductivity and electron mobility along with recombination resistance at the solid liquid interface, the transmission line model with reflecting boundary condition was applied to impedance data across a range of potentials.[52] Originally used to decouple transport and transfer properties of TiO_2 by Fabregat-Santiago *et al.*, this model has been applied widely to mesoporous TiO_2 and ZnO NRs,[31,37,53,54] in electrolyte and in dye sensitised solar cells.

Raw Nyquist plots along with their model fits can be found for sample 0.4% Y in Fig. 4. In the potential region <0.2 V_{RHE}, the ZnO is conductive and can be fit by a simple RQ circuit shown in Fig. 4A (inset) as it displayed a single arc, yielding the chemical capacitance, C_μ, and recombination resistance, R_R. However, from 0.3 to 0.8 V, shown in Fig. 4B, the Nyquist plots displayed a visible upward bend which is clearly visible in the magnified plots in Fig. 4C. This is a typical transmission line behaviour. The bend separates two distinct regions. The high frequency region is dominated by the electron transport resistance, R_T, while the low frequency region determined by the recombination resistance at the interface, R_R at the interface. To fit the data that includes both the transport resistance and the recombination resistance, the transmission line model was used, displayed in the inset of Fig. 4B. R_T is the product of NR length L and r_T, whereas R_R is defined as r_R / L.

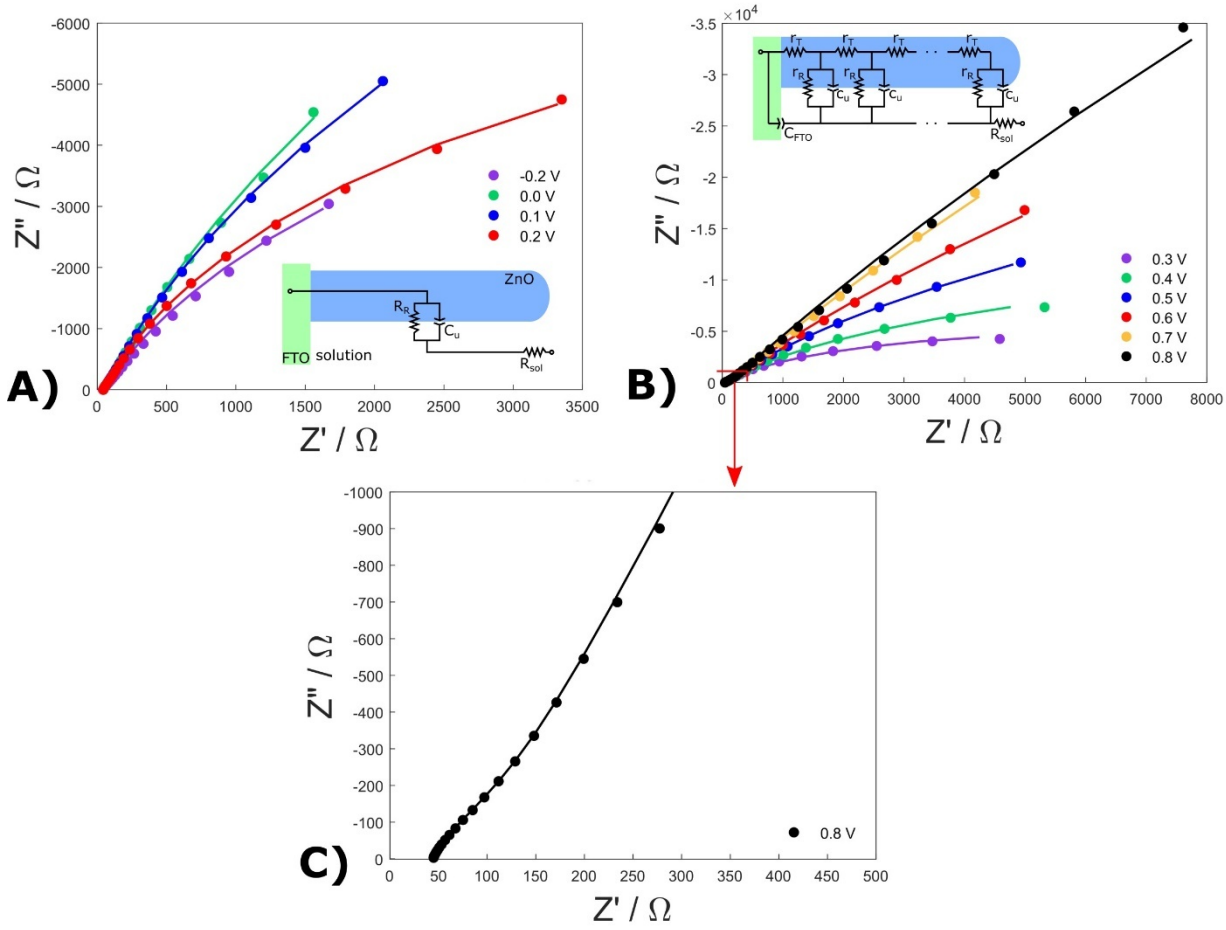

Figure 4: A) and B) Raw experimental Nyquist data (points) and simulated model fits (lines) from 0.04% Y sample. The models used are shown in the insets for the potential ranges 0.3 to 0.8 and -0.2 to 0.2 V_{RHE} respectively. C) Expanded view of the plot indicating the high frequency diffusion region below the 'knee'.

The analysis of this region is challenging to obtain reliable values of transport resistance R_T with highly doped conductive ZnO,[54] although, in this study a noticeable high frequency feature can be distinguished in all the samples. However, in the high frequency region, the constant phase angles of all samples are is significantly larger than 45°. Similar behaviour was reported and is likely due to the added capacitance from the FTO.[31,38,55] The experimental data and simulated fits for the remaining samples are shown in Fig. S4-6.

Once transport resistance R_T is determined, electron conductivity σ_n can be calculated from a cylindrical model for the vertically aligned hexagonal nanorods.

$$\sigma_n = \frac{L}{R_T \pi r^2 \rho} \tag{3}$$

Where L is the nanorod length, r the radius and ρ the number of NRs per unit area, all determined by SEM. σ_n is a bulk material parameter which describes the emergent electron transport properties regardless of geometry. Typically this value depends on the product of electron mobility, μ_n, and free carrier concentration related to N_D. Electron mobility describes the ease of electron drift in the presence of an electric field. It can be calculated via transmission line parameters R_T, C_μ and constant phase element exponent γ with Equation 4.[31]

$$\mu_n = \frac{eL^2}{kT(R_T C_\mu)^{1/\gamma}} \tag{4}$$

The mobilities calculated by this technique often display different character to those determined by hall conductivity measurements due to the nature of trap limited diffusion.[56]

The transport properties of the NRs, including conductivity, charge mobility and charge recombination resistance, determined by transmission line model as a function of potential for samples at different dopant concentrations are shown in Fig. 5A-C. The conductivities for all samples decreases as the potential increases, due to the positive potential pushing the Fermi level below the conduction band minimum, causing a significant drop in electron concentration.[11]

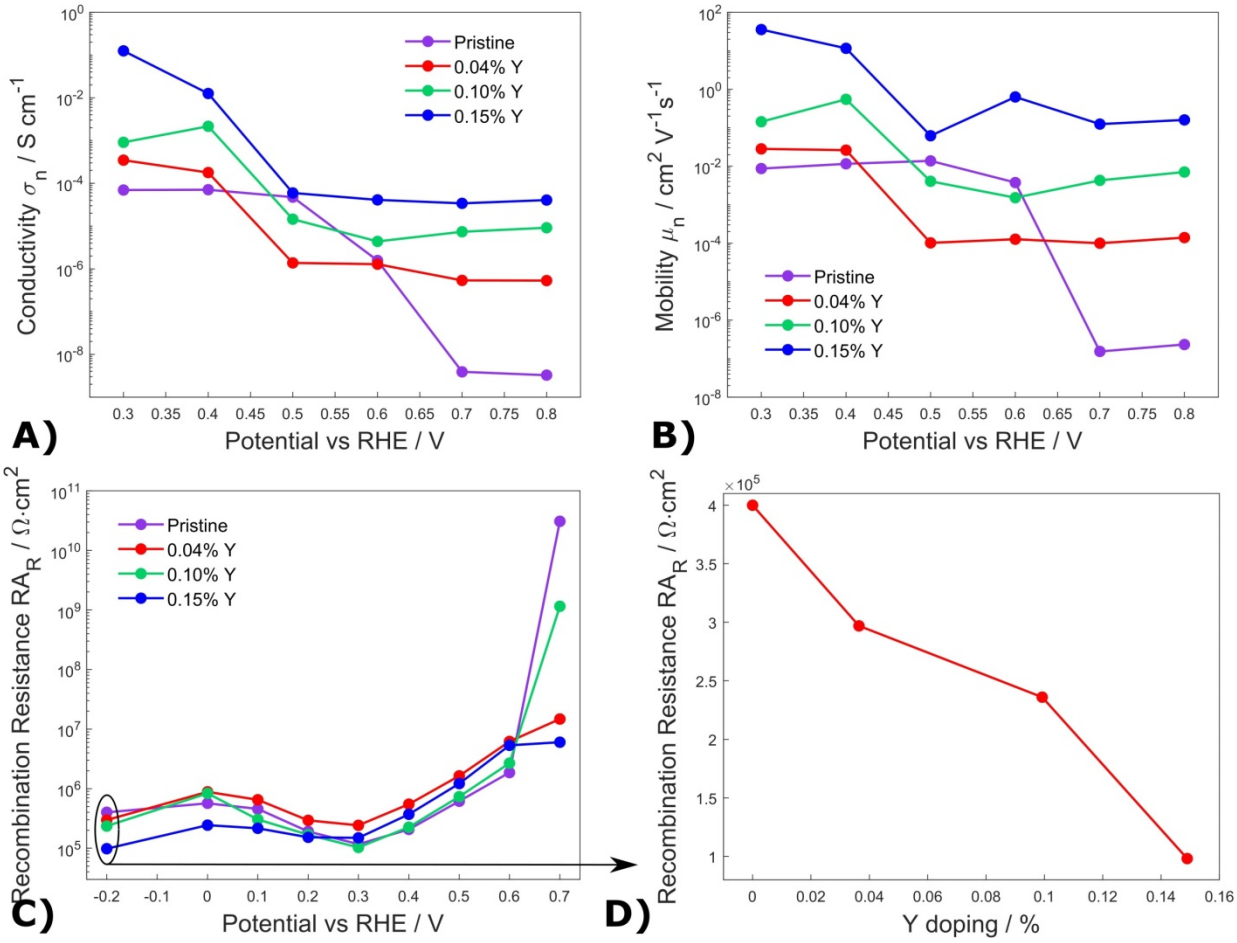

Figure 5: A) Shows the conductivity of the samples. B) Electron mobility through the transmission line potential region, and C) area normalised recombination resistance, RA_R. D) Normalised recombination resistance of the samples measured at -0.2 V_{RHE}.

A clear increase in conductivity is observed in the doped samples, at 0.3 and 0.8 V, 0.15% Y sample showed 1000 and 10,000 fold increase in conductivity over the pristine sample, respectively. This is too large to be explained by an 80% gain in dopant density (Fig. 3B), but an accompanying enhancement in electron mobility.

The electron mobility of the samples has been calculated using Eq. 4 and shown in Fig. 5B. The variation of electron mobility as a function of dopant concentration, suggests trap-

limited diffusion, where electrons from defect states are injected into the conduction band.[56] Higher electron concentration associated with defect states leads to increased mobility in ZnO NRs by neutralising charge traps.[8]

The recombination resistance R_R, inversely proportional to recombination current flux,[57] is normalised by multiplication by the sample surface area, RA_R,[58] and displayed in Fig. 5C. A similar trend can be observed for all the samples, beginning low, negative of V_{FB} and rising rapidly up to 0.7 V_{RHE}. At -0.2 V_{RHE} when the ZnO yields a metallic response, a monotic decrease in R_R is observed with doping, Fig. 5D. Higher doping of yttrium causes greater recombination of electron hole pairs due to the dopant ions acting as recombination centres in the bulk and at the surface.[59] As expected the pristine sample shows a dramatic rise in R_R towards higher potentials past the onset, and 0.15% retains the fastest recombination. Somewhat unexpected is the reversal of recombination rates of 0.10% and 0.04% samples at 0.7 V_{RHE}. This is likely due to the more negative position of V_{FB} for the 0.10% samples, promoting charge transfer across the junction and restricting recombination current.

The effect of yttrium doping on light absorption was measured using UV-Vis reflectance spectroscopy. Band gaps were calculated using the Kubelka-Munk function *F(R)*, detailed in section 1.2 in the supporting information.[60] This was followed by the use of Tauc plots for the n-type semiconductors, shown in Fig. 6A, with B presenting a decreased band gap with yttrium doping.[61]

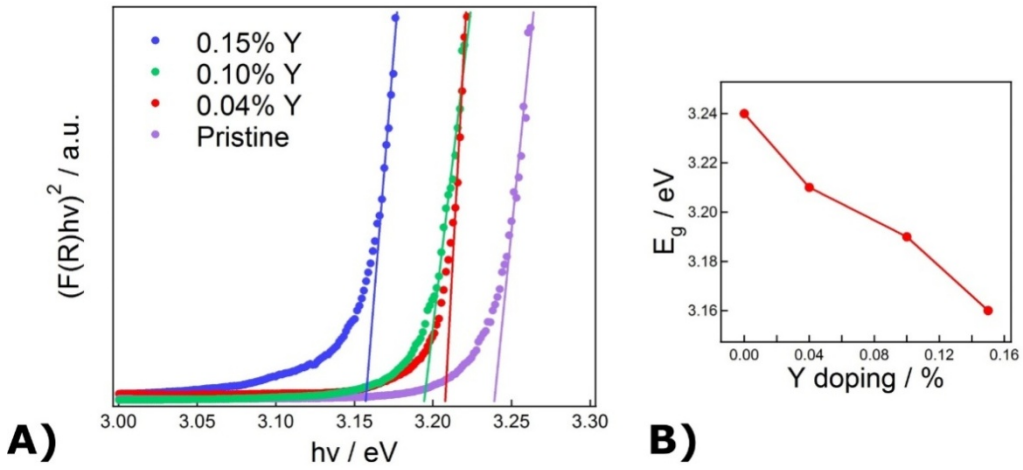

Figure 6: A) Tauc plot of the samples along with extrapolated linear regions for determination of band gap. B) Band gap energy against doping, determined by Tauc plot.

The band gap behaviour is in good agreement with our previous measurements made on hydrothermal bath deposited Y doped ZnO NRs.[23] The decrease in the band gap energy as the dopant concentration increases is due to additional donor states formed close to the conduction band minimum within the band gap of ZnO.[62] This requires lower energy photons to promote valence band electrons to these states resulting in greater visible light absorption. Though small, this band gap reduction is advantageous to the PEC water splitting performance of the samples, accessing a greater portion of the visible light in the solar spectrum.

PL spectroscopy was performed to confirm recombination rates and the electronic defect structure of the samples. An excitation of 320 nm was used, and the spectra were normalised using the absorbance of each sample at this wavelength. Greater intensity across the entire spectra was observed with higher yttrium concentration, confirming the trend in recombination resistance R_R determined by EIS. Faster electron hole recombination yields more intense near-band-edge (NBE) emission as a result of the interaction of excitons with

substitutional yttrium, Y_{Zn}. No new distinct peaks can be seen from Y_{Zn} doping, confirming that it is a shallow donor. However, interstitial yttrium Y_i may be responsible for larger peaks across the spectra due to its interaction with native point defects. The integrated spectra, Fig. 7C, reveals the increase in PL intensities as doping levels increases, negatively impacting water splitting rate.

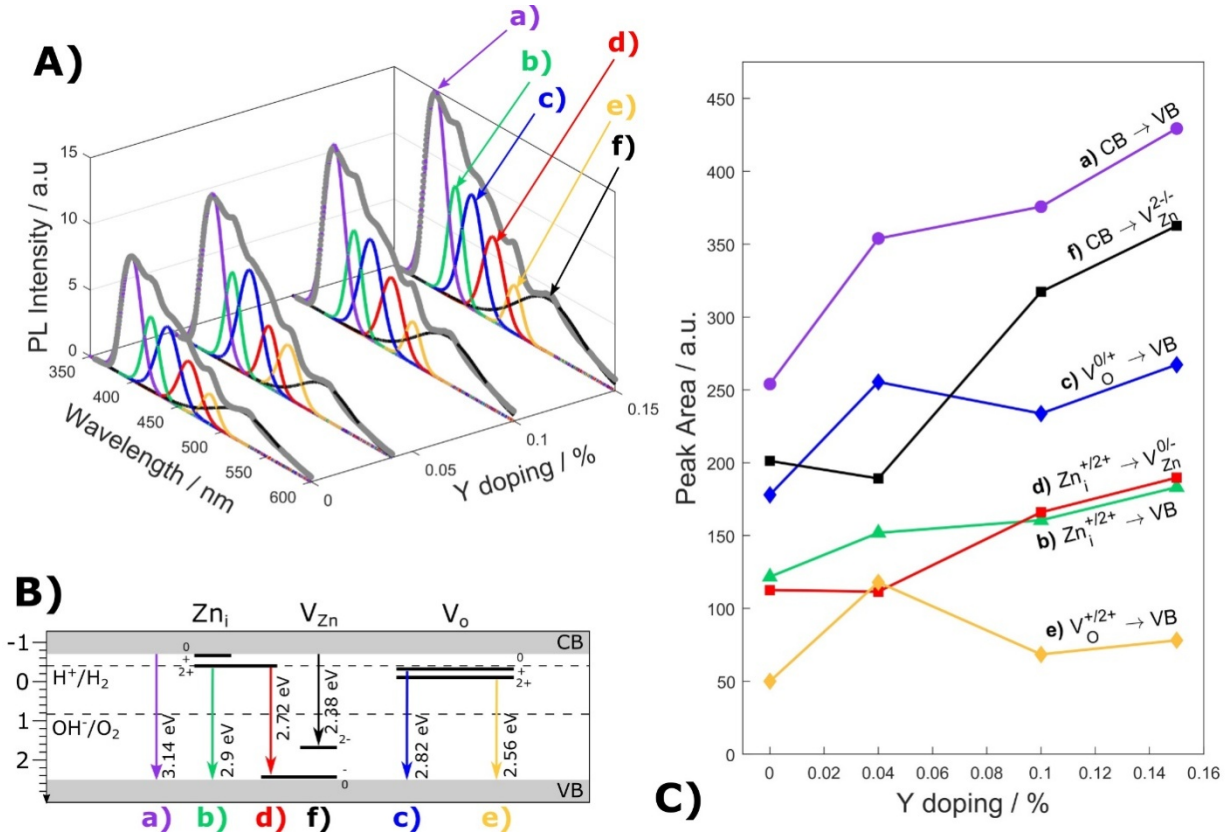

Figure 7: A) Expanded view of PL spectra, allowing the changes in peaks a-f to be observed. B) Transitions assigned to each peak, and finally C) Integrated peak intensity for each of the transitions at different Y concentrations.

Six distinct peaks are observed forming the PL spectra, centred at 398, 419, 441, 462, 485 and 528 nm, labelled a-f) in Fig. 7A). The spectra were analysed with non-linear least square

fitting to resolve the PL emission intensity of each peak which is related to the corresponding defect concentration. The assignment of the emission peaks is shown in Fig. 7B. The leading emission peak at 398 nm, peak a, is assigned to the NBE. Peak b is associated with donor level introduced by Zn_i.[63,64] Peaks c and e occur from the two charge state transitions of V_O.[50,64] Peak d is due to an inter-defect transition from Zn_i to the $V_{Zn}^{-/0}$ state, 0.18 eV above the valence band,[50] and finally f originates from the Zn^{2+} vacancies V_{Zn}.[50,63,65]

The intensity of NBE peak is seen to increase from pristine to 0.15% sample, following the trend seen in the total PL integrals due to faster exciton recombination rate.[52] A subtle rise in intensity for peak b is also observed, however it is unlikely due to a higher concentration of Zn_i with increased Y doping in the NRs. Rather, this defect is probably being fed by a more populous conduction band. More prominent effects are seen in peaks c-f. An initial drop in peak f is observed, followed by substantial increase in intensity due to increasing population of V_{Zn} as a result of Y doping. The initial decrease in V_{Zn} concentration at low level doping (from pristine to 0.04% Y) is due to the filling of V_{Zn} with Y_{Zn} substituting a deep acceptor state with a shallow donor. Further increase in the Y doping will lead to the increase of interstitial Y^{3+} which decreases the R_R with enhanced electron mobility (Fig. 5D).[51] Consequently, this effect increases the formation energy of V_O, leading to a decline in peak c and e for Y doping of 0.1% and higher.[50] It is important to note that the PL spectra intensity could be significantly affected by the film thickness and the wavelength of the excitation sources. However, the light penetration depth of the absorbed and emitted photons is normally small,[66] in comparison with the thickness of our samples (>1.6 μm). Hence the film thickness is less likely to affect the PL intensities. Meanwhile, a UV light with fixed wavelength of 300

nm was used for all PL measurements. The light absorption in this region by Y doped ZnO is normally featureless. Therefore, the PL intensity can be exclusively contributed from the charge recombination effects. Furthermore, the peaks observed only yield data on deep electronic states causing radiative transitions. Shallow states, such as those likely caused by yttrium dopants, introduce vibrational states, undetected by this technique.[67]

3.3 Water Splitting Performance

The measured photocurrent densities of the pristine and yttrium doped samples display their PEC water splitting abilities, found in Fig. 8A. Photocurrent density uniformly increased across all samples with positive bias to a maximum of 0.84 mA cm^{-2} for the optimised 0.1% Y sample at 1.23 V_{RHE}. This represents a 23% enhancement from the undoped sample, due to improved charge transportation from higher conductivity. This value is greater than those achieved by doping ZnO NRs with N,[68] Na[14] and Al,[15] which achieved photocurrent of 0.3, 0.5 and 0.3 mA cm^{-2}, respectively, at the same bias. Furthermore the rapid microwave synthesis used in this work,[40] displays over double the photocurrent achieved by carbon nitride coated YZnO (0.4 mA cm^{-2} at 1.23 V_{RHE}).[30] Although, the photolysis in this work falls short of doped and coated core-shell structured photoanodes, which have much improved visible light absorption. With hydrogen doping or hematite coating,[69,70] photocurrents of 1.00 or 1.27 mA cm^{-2} were achieved, respectively. In order to utilise ZnO in higher performing photolysis, its major shortcoming of low visible light absorption must be overcome. One solution is the decoration with noble metal plasmonic nanoparticles, such as the gold tipped match-like structures produced by Wu *et al.*[12] Alternatively low band gap, CdS and CdSe

quantum dots have been used in conjunction with ZnO for enhanced solar performance.[71,72] Hence, visible light sensitisation offers potential for further enhancing the YZnO as a photoanode in future.

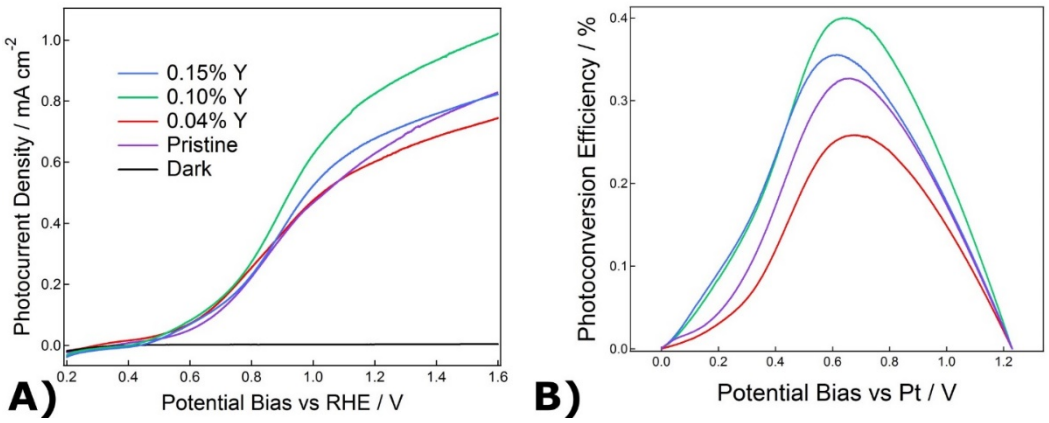

Figure 8: A) The photocurrent density curves against potential bias V_{RHE}, and B) the photoconversion efficiency.

Calculated photoconversion efficiency, η, curves are displayed in Fig. 8B, The equation used is the ratio of output electrochemical power to input solar power densities, P, in Eq. 5.[73]

$$\eta = \frac{J(1.23 - V)}{P} \tag{5}$$

Where J is the photocurrent density and V is the applied bias vs the platinum electrode. The highest efficiency of 0.4%, giving a 47% enhancement over the pristine NRs, was achieved at 0.1% Y doping. Further increases to the doping level leads to a high density of defects on the NR surface which effectively forms recombination centres as confirmed with both EIS and PL measurements. Hence, it is important to optimise the appropriate defects level while maintaining the electron transportation benefits. The stability of the photoanode is

shown in Fig. S7. The photocurrent was monitored at constant potential of 1.23 V_{RHE}. There is no degradation after 5 minutes of stepped illumination.

The microwave synthesis also performs favourably in comparison to yttrium doped zinc oxide nanorods synthesised by conventional hydrothermal method. Solar water splitting data of hydrothermal NRs, both doped and undoped, can be seen in Figure S8. It is clear that yttrium doping once again leads to more favourable performance. However, the photocurrent measured at 1.23 V_{RHE} from hydrothermal method (0.22 mA/cm^2) is still much lower than those produced from the this novel MW method (0.84 mA/cm^2). On the other hand, both methods have achieved similar yttrium doping atomic concentration, as seen in Table S1. This observation confirms that the NRs synthesised in MW method must have other effects which are critical for the higher PEC performance.

The MW samples significantly outperform hydrothermal samples possibly due to native point defect states that contribute to both light absorption and dopant density as outlined in our previous work.[40] Furthermore, hydrothermal ZnO NRs are crippled by surface hydroxide groups acting as recombination centres due to the high pH synthesis. To overcome this, Baek *et al.* annealed hydrothermal synthesised samples produced by this method in a vacuum at 700°C for restoring performance.[74]

Also important, it was found that the Y doping significantly improves the resistance to photocorrosion. Under continuous operation, the photo current was measured at 1.23 V_{RHE}, shown in Figure S9. The pristine sample decayed to half performance after 12 minutes while it took 3 times longer for the 0.1%Y sample. The mechanism for this is unclear and beyond

the scope of this study. Perhaps a thin layer of Y_2O_3 was formed on the surface of the NRs, which decreases the PEC corrosive reaction. This further advantage cements yttrium as a stand out dopant for ZnO in solar applications going forward.

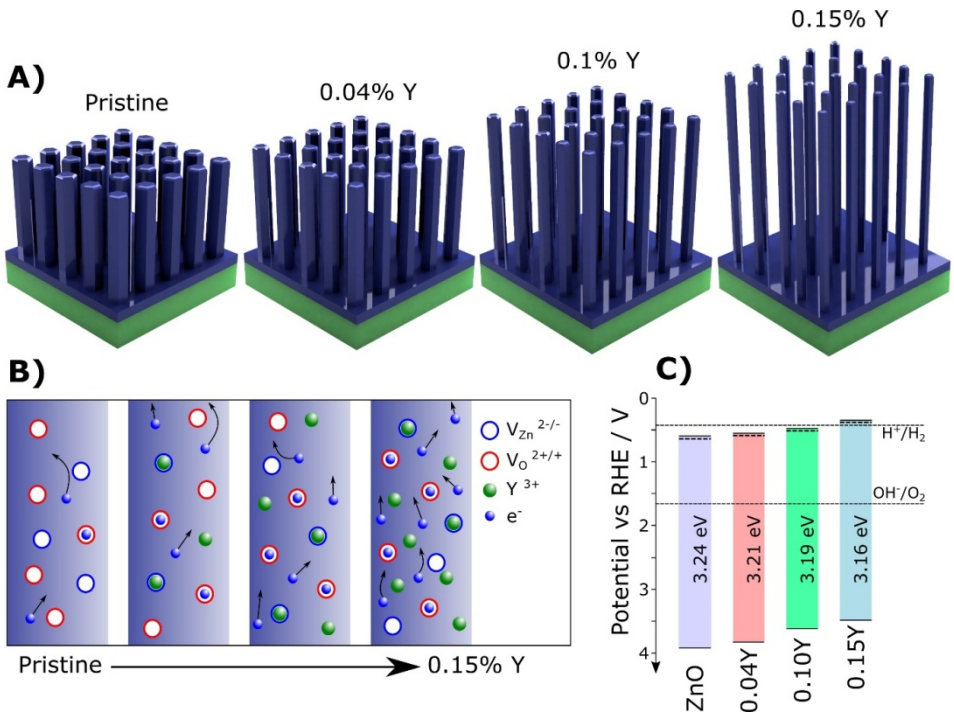

Figure 9: A) Morphological benefits of Y doping, B) Schematic explaining increased electron mobility from trap filling, and C) measured band edge and E_F positions typical of ZnO,[75] with redox potentials at standard hydrogen potential, equivalent to pH=0.

The mechanism for the high efficiency of Y doped ZnO are explained in terms of morphological and electronic effects in Y doping. Firstly, the Y doping results in the reduction of NR diameter with increased NR length. Hence, the effective surface area is increased, Fig. 9A. Longer NRs also provide greater optical depth for light absorption. Secondly, the great increase in electron mobility provides improved electron transport. This is

especially important for nanomaterials with vertically aligned morphology. As the optical depth increases with the increased NR length, photoexcited electrons also need to travel significant longer distance. The improved electron transportation reduces the energy cost for electrons travelling from the NR surface to the FTO conductive layer. Although increasing Y doping leads to significantly improved σ_n, reduced R_R is the cost as the ZnO NR crystals become too defective. This has been confirmed with both EIS and PL measurements. The highest doped sample, 0.15% Y, presents a reduction in efficiency from 0.1% Y as the anode is stifled by the high rate of recombination. Hence, the doping level must be controlled in order to balance increased σ_n against increased recombination rate.

Thirdly, a reduction in electronic band gap caused by Y doping would allow the ZnO to absorb more visible light. The reduction of band gap energy was identified by UV-Vis reflection spectroscopy as a result of trap filling, illustrated in Fig. 9B. This is particularly important when utilising solar energy with ZnO, since solar irradiance becomes much more intense with shifting wavelength from UV to blue visible. Fourthly, the negative shift in flat band potential provides an earlier onset potential for solar water splitting. This was observed from a morphology-corrected Mott-Schottky analysis, shown in Fig. 3B. The effects of doping on the band alignment for water splitting is shown in Fig. 9C.[76] The 0.04% Y sample shows the lowest performance. This is possibly due to its greater recombination rate without significant enhancement of electron transport.

Conclusion

In conclusion, for the first time bare yttrium doped zinc oxide NRs have been synthesised for application to solar water splitting. Samples were prepared with 0, 0.04, 0.1

and 0.15% yttrium incorporation into the structures. The microwave synthesised NRs displayed more favourable morphology with a reduction in radius, along with enlarged crystal domain size implying the penetration of yttrium into the lattice. The Y acted as a shallow n-type donor, increasing the donor density in the ZnO NRs leading to increased conductivity determined by transmission line model. There was also a significant gain in electron mobility due to the filling of trap states, leading to a 1000 fold improvement from pristine ZnO. The electronic effects of higher Y concentration were confirmed by UV-Vis reflectance spectroscopy, reducing the band gap due to new states at the edge of the conduction band. PL spectroscopy displayed accompanying recombination rate increase along with the reduction in some crystal defects by deconvoluting the transition peaks. Yttrium addition, overall, led to higher concentrations of V_{Zn} and less V_O by altering their respective formation energies, further impacting mobility and increasing hole concentration. The superior transport properties of YZnO resulted in a 47% enhancement of photoconversion efficiency, indicating their promise as electron transport materials in solar cells and coated photoanodes.

Supporting Information

Shows nanorod length and diameter plotted against doping, cross sectional SEM images of various doping alongside diameter histograms, close-up 002 ZnO XRD peaks, the derivation of Equation (2), the raw EIS data in Nyquist plots with fitted models, raw transmission model parameters, the Kubelka Munk function, chopped chronoamperometry curves performance of typical hydrothermal ZnO NRs and finally long term photocorrosion.

Author Information

Corresponding Author:

*Qiao.chen@sussex.ac.uk

ORCID

Daniel Commandeur: 0000-0002-7179-2370

John Spencer: 0000-0001-5231-8836

Qiao Chen : 0000-0001-5424-4818

The authors declare no competing financial interest.

Acknowledgements

The authors would like to thank the University of Sussex, School of Life Sciences for the funding of this work.

References

(1) Demirbas, A. Future Hydrogen Economy and Policy. *Energy Sources, Part B Econ. Planning, Policy* **2017**, *12* (2), 172–181.

(2) Fujishima, A.; Honda, K. Electrochemical Photolysis of Water at a Semiconductor Electrode. *Nature* **1972**, *238* (5358), 37–38.

(3) Walter, M. G.; Warren, E. L.; McKone, J. R.; Boettcher, S. W.; Mi, Q.; Santori, E. A.; Lewis, N. S. Solar Water Splitting Cells. *Chem. Rev.* **2010**, *110* (11), 6446–6473.

(4) Chen, X.; Shen, S.; Guo, L.; Mao, S. S. Semiconductor-Based Photocatalytic Hydrogen Generation. *Chem. Rev.* **2010**, *110* (11), 6503–6570.

(5) Ballestas-Barrientos, A.; Li, X.; Yick, S.; Masters, A. F.; Maschmeyer, T. Optimised Heterojunctions between [100]-Oriented Rutile TiO_2 Arrays and {001} Faceted Anatase Nanodomains for Enhanced Photoelectrochemical Activity. *Sustain. Energy Fuels* **2018**, *2* (7), 1463–1473.

(6) Fang, Y.; Li, X.; Wang, X. Synthesis of Polymeric Carbon Nitride Films with Adhesive Interfaces for Solar Water Splitting Devices. *ACS Catal.* **2018**, *8* (9), 8774–8780.

(7) Yu, Q.; Cao, C. B. ZnO Nanorod Arrays for Photoelectrochemical Cells. *J. Nanosci. Nanotechnol.* **2012**, *12* (5), 3984–3989.

(8) Baxter, J. B.; Schmuttenmaer, C. A. Conductivity of ZnO Nanowires, Nanoparticles,

and Thin Films Using Time-Resolved Terahertz Spectroscopy. *J. Phys. Chem. B* **2006**, *110* (50), 25229–25239.

(9) Choi, S. Y.; Kim, C.-D.; Han, D. S.; Park, H. Facilitating Hole Transfer on Electrochemically Synthesized P-Type $CuAlO_2$ Films for Efficient Solar Hydrogen Production from Water. *J. Mater. Chem. A* **2017**, *5* (21), 10165–10172.

(10) Pagano, R.; Quarta, A.; Pal, S.; Licciulli, A.; Valli, L.; Bettini, S. Enhanced Solar-Driven Applications of ZnO@Ag Patchy Nanoparticles. *J. Phys. Chem. C* **2017**, *121* (48), 27199–27206.

(11) Martinson, A. B. F.; Goes, M. S.; Fabregat-Santiago, F.; Bisquert, J.; Pellin, M. J.; Hupp, J. T. Electron Transport in Dye-Sensitized Solar Cells Based on Zno Nanotubes: Evidence for Highly Efficient Charge Collection and Exceptionally Rapid Dynamics. *J. Phys. Chem. A* **2009**, *113* (16), 4015–4021.

(12) Wu, M.; Chen, W. J.; Shen, Y. H.; Huang, F. Z.; Li, C. H.; Li, S. K. In Situ Growth of Matchlike ZnO/Au Plasmonic Heterostructure for Enhanced Photoelectrochemical Water Splitting. *ACS Appl. Mater. Interfaces* **2014**, *6* (17), 15052–15060.

(13) Allagui, A.; Alawadhi, H.; Alkaaby, M.; Gaidi, M.; Mostafa, K.; Abdulaziz, Y. Mott-Schottky Analysis of Flower-like ZnO Microstructures with Constant Phase Element Behavior. *Phys. Status Solidi Appl. Mater. Sci.* **2016**, *213* (1), 139–145.

(14) Lee, W. C.; Canciani, G. E.; Alwhshe, B. O. S.; Chen, Q. Enhanced

Photoelectrochemical Water Oxidation by ZnxMyO (M = Ni, Co, K, Na) Nanorod Arrays. *Int. J. Hydrogen Energy* **2016**, *41* (1), 123–131.

(15) Xu, Y. F.; Rao, H. S.; Wang, X. D.; Chen, H. Y.; Kuang, D. B.; Su, C. In Situ Formation of Zinc Ferrite Modified Al-Doped ZnO Nanowire Arrays for Solar Water Splitting. *J. Mater. Chem. A* **2016**, *4* (14), 5124–5129.

(16) Kaur, R.; Singh, A. V.; Mehra, R. M. Structural, Electrical and Optical Properties of Sol-Gel Derived Yttrium Doped ZnO Films. *Phys. Status Solidi* **2005**, *202* (6), 1053–1059.

(17) Bai, L. N.; Sun, H. M.; Lian, J. S.; Jiang, Q. Tunable UV Absorption and Mobility of Yttrium-Doped ZnO Using First-Principles Calculations. *Chinese Phys. Lett.* **2012**, *29* (11), 117101.

(18) Yu, Q.; Fu, W.; Yu, C.; Yang, H.; Wei, R.; Sui, Y.; Liu, S.; Liu, Z.; Li, M.; Wang, G.; et al. Structural, Electrical and Optical Properties of Yttrium-Doped ZnO Thin Films Prepared by Sol–Gel Method. *J. Phys. D. Appl. Phys.* **2007**, *40* (18), 5592–5597.

(19) Wen, J. Q.; Zhang, J. M.; Li, Z. Q. Structural and Electronic Properties of Y Doped ZnO with Different Y Concentration. *Opt. - Int. J. Light Electron Opt.* **2018**, *156*, 297–302.

(20) Heo, S.; Sharma, S. K.; Lee, S.; Lee, Y.; Kim, C.; Lee, B.; Lee, H.; Kim, D. Y. Effects of Y Contents on Surface, Structural, Optical, and Electrical Properties for Y-Doped

ZnO Thin Films. *Thin Solid Films* **2014**, *558*, 27–30.

(21) Tsai, Y. Z.; Wang, N. F.; Tseng, M. R.; Hsu, F. H. Transparent Conducting Al and Y Codoped ZnO Thin Film Deposited by DC Sputtering. *Mater. Chem. Phys.* **2010**, *123* (1), 300–303.

(22) Kaur, N.; Sharma, S. K.; Kim, D. Y.; Singh, N. Highly Transparent and Lower Resistivity of Yttrium Doped ZnO Thin Films Grown on Quartz Glass by Sol–Gel Method. *Phys. B Condens. Matter* **2016**, *500*, 179–185.

(23) Lee, W. C.; Fang, Y.; Turner, J. F. C.; Bedi, J. S.; Perry, C. C.; He, H.; Qian, R.; Chen, Q. An Enhanced Gas Ionization Sensor from Y-Doped Vertically Aligned Conductive ZnO Nanorods. *Sensors Actuators, B Chem.* **2016**, *237*, 724–732.

(24) Üzar, N.; Algün, G.; Akçay, N.; Akcan, D.; Arda, L. Structural, Optical, Electrical and Humudity Sensing Properties of (Y/Al) Co-Doped ZnO Thin Films. *J. Mater. Sci. Mater. Electron.* **2017**, *28* (16), 11861–11870.

(25) Wang, N. F.; Tsai, Y. Z.; Tseng, M. R.; Hsu, F. H. A Novel Al-Y Codoped ZnO Thin Film as Anode for Organic Light Emitting Diode. *Integr. Ferroelectr.* **2013**, *143* (1), 17–23.

(26) Zheng, J. H.; Song, J. L.; Jiang, Q.; Lian, J. S. Enhanced UV Emission of Y-Doped ZnO Nanoparticles. *Appl. Surf. Sci.* **2012**, *258* (18), 6735–6738.

(27) Parangusan, H.; Ponnamma, D.; Al-Maadeed, M. A. A.; Marimuthu, A. Nanoflower-

like Yttrium-Doped ZnO Photocatalyst for the Degradation of Methylene Blue Dye. *Photochem. Photobiol.* **2018**, *94* (2), 237–246.

(28) Zheng, J. H.; Niu, S. F.; Zheng, R. Y.; Zhang, W. X.; Yu, P. F. Synthesis and Characterization of AL-Y Co-Doped ZnO Powders with High Photocatalytic Properties. *Optoelectron. Adv. Mater. Rapid Commun.* **2016**, *10* (3–4), 222–227.

(29) Huo, J.; Fang, L.; Lei, Y.; Zeng, G.; Zeng, H. Facile Preparation of Yttrium and Aluminum Co-Doped ZnO via a Sol–Gel Route for Photocatalytic Hydrogen Production. *J. Mater. Chem. A* **2014**, *2* (29), 11040–11044.

(30) Fang, Y.; Xu, Y.; Li, X.; Ma, Y.; Wang, X. Coating Polymeric Carbon Nitride Photoanodes on Conductive Y:ZnO Nanorod Arrays for Overall Water Splitting. *Angew. Chemie Int. Ed.* **2018**, *57* (31), 9749–9753.

(31) Fabregat-Santiago, F.; Garcia-Belmonte, G.; Bisquert, J.; Zaban, A.; Salvador, P. Decoupling of Transport, Charge Storage, and Interfacial Charge Transfer in the Nanocrystalline TiO_2/Electrolyte System by Impedance Methods. *J. Phys. Chem. B* **2002**, *106* (2), 334–339.

(32) Cummings, C. Y.; Marken, F.; Peter, L. M.; Upul Wijayantha, K. G.; Tahir, A. A. New Insights into Water Splitting at Mesoporous α-Fe_2O_3 Films: A Study by Modulated Transmittance and Impedance Spectroscopies. *J. Am. Chem. Soc.* **2012**, *134* (2), 1228–1234.

(33) Garcia-Belmonte, G.; Munar, A.; Barea, E. M.; Bisquert, J.; Ugarte, I.; Pacios, R. Charge Carrier Mobility and Lifetime of Organic Bulk Heterojunctions Analyzed by Impedance Spectroscopy. *Org. Electron. physics, Mater. Appl.* **2008**, *9* (5), 847–851.

(34) Wang, Q.; Ito, S.; Grätzel, M.; Fabregat-Santiago, F.; Mora-Seró, I.; Bisquert, J.; Bessho, T.; Imai, H. Characteristics of High Efficiency Dye-Sensitized Solar Cells †. *J. Phys. Chem. B* **2006**, *110* (50), 25210–25221.

(35) Sacco, A. Electrochemical Impedance Spectroscopy: Fundamentals and Application in Dye-Sensitized Solar Cells. *Renew. Sustain. Energy Rev.* **2017**, *79*, 814–829.

(36) Fabregat-Santiago, F.; Bisquert, J.; Garcia-Belmonte, G.; Boschloo, G.; Hagfeldt, A. Influence of Electrolyte in Transport and Recombination in Dye-Sensitized Solar Cells Studied by Impedance Spectroscopy. *Sol. Energy Mater. Sol. Cells* **2005**, *87* (1–4), 117–131.

(37) Dualeh, A.; Moehl, T.; Tétreault, N.; Teuscher, J.; Gao, P.; Nazeeruddin, M. K.; Grätzel, M. Impedance Spectroscopic Analysis of Lead Iodide Perovskite-Sensitized Solid-State Solar Cells. *ACS Nano* **2014**, *8* (1), 362–373.

(38) Dehghan Nayeri, F.; Kolahdouz, M.; Asl-Soleimani, E.; Mohajerzadeh, S. Low Temperature Carving of ZnO Nanorods into Nanotubes for Dye-Sensitized Solar Cell Application. *J. Alloys Compd.* **2015**, *633*, 359–365.

(39) Lee, W. C.; Fang, Y.; Kler, R.; Canciani, G. E.; Draper, T. C.; Al-Abdullah, Z. T. Y.;

Alfadul, S. M.; Perry, C. C.; He, H.; Chen, Q. Marangoni Ring-Templated Vertically Aligned ZnO Nanotube Arrays with Enhanced Photocatalytic Hydrogen Production. *Mater. Chem. Phys.* **2015**, *149–150*, 12–16.

(40) Commandeur, D.; Brown, G.; Hills, E.; Spencer, J.; Chen, Q. Defect-Rich ZnO Nanorod Arrays for Efficient Solar Water Splitting. *ACS Appl. Nano Mater.* **2019**, *2* (3), 1570–1578.

(41) Nakajima, T.; Hagino, A.; Nakamura, T.; Tsuchiya, T.; Sayama, K. WO 3 Nanosponge Photoanodes with High Applied Bias Photon-to-Current Efficiency for Solar Hydrogen and Peroxydisulfate Production. *J. Mater. Chem. A* **2016**, *4* (45), 17809–17818.

(42) Modestino, M. A.; Hashemi, S. M. H.; Haussener, S. Mass Transport Aspects of Electrochemical Solar-Hydrogen Generation. *Energy Environ. Sci.* **2016**, *9* (5), 1533–1551.

(43) Kumar, P.; Singh, V.; Sharma, V.; Rana, G.; Malik, H. K.; Asokan, K. Investigation of Phase Segregation in Yttrium Doped Zinc Oxide. *Ceram. Int.* **2015**, *41* (5), 6734–6739.

(44) Kara, I.; Yildiz, A.; Yildiz, G.; Dogan, B.; Serin, N.; Serin, T. Al and X (Sn, Cu, In) Co-Doped ZnO Nanocrystals. *J. Mater. Sci. Mater. Electron.* **2016**, *27* (6), 6179–6182.

(45) Shannon, R. D. Revised Effective Ionic Radii and Systematic Studies of Interatomic Distances in Halides and Chalcogenides. *Acta Crystallogr. Sect. A* **1976**, *32* (5), 751–767.

(46) Memming, R. *Semiconductor Electrochemistry*; Wiley-VCH Verlag GmbH: Weinheim, Germany, 2000.

(47) Mora-Seró, I.; Fabregat-Santiago, F.; Denier, B.; Bisquert, J.; Tena-Zaera, R.; Elias, J.; Lévy-Clément, C. Determination of Carrier Density of ZnO Nanowires by Electrochemical Techniques. *Appl. Phys. Lett.* **2006**, *89* (20), 203117.

(48) Zhao, Y.; Liu, Z.; Yang, H.; Li, T.; Yang, P. Approach Using the Electrical Structure and Optical Properties of Aluminium-Doped Zinc Oxide for Solar Cells. *RSC Adv.* **2016**, *6* (112), 110943–110950.

(49) Sachet, E.; Shelton, C. T.; Harris, J. S.; Gaddy, B. E.; Irving, D. L.; Curtarolo, S.; Donovan, B. F.; Hopkins, P. E.; Sharma, P. A.; Sharma, A. L.; et al. Dysprosium-Doped Cadmium Oxide as a Gateway Material for Mid-Infrared Plasmonics. *Nat. Mater.* **2015**, *14* (4), 414–420.

(50) Janotti, A.; Van De Walle, C. G. Native Point Defects in ZnO. *Phys. Rev. B - Condens. Matter Mater. Phys.* **2007**, *76* (16), 1–22.

(51) Kelley, K. P.; Sachet, E.; Shelton, C. T.; Maria, J.-P. High Mobility Yttrium Doped Cadmium Oxide Thin Films. *APL Mater.* **2017**, *5* (7), 076105.

(52) Bisquert, J. Theory of the Impedance of Electron Diffusion and Recombination in a Thin Layer. *J. Phys. Chem. B* **2002**, *106* (2), 325–333.

(53) Qiu, J.; Li, X.; Zhuge, F.; Gan, X.; Gao, X.; He, W.; Park, S. J.; Kim, H. K.; Hwang, Y.

H. Solution-Derived 40 μm Vertically Aligned ZnO Nanowire Arrays as Photoelectrodes in Dye-Sensitized Solar Cells. *Nanotechnology* **2010**, *21* (19), 195602.

(54) Guillén, E.; Azaceta, E.; Peter, L. M.; Zukal, A.; Tena-Zaera, R.; Anta, J. A. ZnO Solar Cells with an Indoline Sensitizer: A Comparison between Nanoparticulate Films and Electrodeposited Nanowire Arrays. *Energy Environ. Sci.* **2011**, *4* (9), 3400.

(55) Wijeratne, K.; Seneviratne, V. A.; Bandara, J. Optimization and Tuning of the Aspect Ratio of Hydrothermally Grown ZnO Nanorods by Varying the Hydrothermal Temperature and Their Electron Transport Properties. *EPJ Appl. Phys.* **2015**, *69* (1), 10403.

(56) Bisquert, J.; Zaban, A. The Trap-Limited Diffusivity of Electrons in Nanoporous Semiconductor Networks Permeated with a Conductive Phase. *Appl. Phys. A Mater. Sci. Process.* **2003**, *77* (3–4), 507–514.

(57) Gonzalez-Pedro, V.; Juarez-Perez, E. J.; Arsyad, W.-S.; Barea, E. M.; Fabregat-Santiago, F.; Mora-Sero, I.; Bisquert, J. General Working Principles of CH_3NH_3 PbX_3 Perovskite Solar Cells. *Nano Lett.* **2014**, *14* (2), 888–893.

(58) Bisquert, J.; Mora-Sero, I.; Fabregat-Santiago, F. Diffusion-Recombination Impedance Model for Solar Cells with Disorder and Nonlinear Recombination. *ChemElectroChem* **2014**, *1* (1), 289–296.

(59) Park, S. U.; Koh, J. H. Electrical and Optical Properties of in and Al Doped ZnO Thin

Film. *Electron. Mater. Lett.* **2013**, *9* (4), 493–496.

(60) Kubelka, P., Munk, F. Ein Beitrag Zur Optik Der Farbanstriche. *Z. Techn. Phys.* **1931**, *12*, 593–601.

(61) Tauc, J. Optical Properties and Electronic Structure of Amorphous Ge and Si. *Mater. Res. Bull.* **1968**, *3* (1), 37–46.

(62) Jabbari, V.; Hamadanian, M.; Shamshiri, M.; Villagrán, D. Band Gap and Schottky Barrier Engineered Photocatalyst with Promising Solar Light Activity for Water Remediation. *RSC Adv.* **2016**, *6* (19), 15678–15685.

(63) Lin, B.; Fu, Z.; Jia, Y. Green Luminescent Center in Undoped Zinc Oxide Films Deposited on Silicon Substrates. *Appl. Phys. Lett.* **2001**, *79* (7), 943.

(64) Cheng, P.; Li, S.; Zhang, L.; Li, J. Characterization of Intrinsic Donor Defects in ZnO Ceramics by Dielectric Spectroscopy. *Appl. Phys. Lett.* **2008**, *93* (1), 111–114.

(65) Sekiguchi, T.; Ohashi, N.; Terada, Y. Effect of Hydrogenation on ZnO Luminescence. *Jpn. J. Appl. Phys.* **1997**, *36* (Part 2, No. 3A), L289–L291.

(66) Uma Sangari, N.; Chitra Devi, S. Synthesis and Characterization of Nano ZnO Rods via Microwave Assisted Chemical Precipitation Method. *J. Solid State Chem.* **2013**, *197*, 483–488.

(67) Chiang, Y. H.; Li, M. H.; Cheng, H. M.; Shen, P. S.; Chen, P. Mixed Cation Thiocyanate-Based Pseudohalide Perovskite Solar Cells with High Efficiency and

Stability. *ACS Appl. Mater. Interfaces* **2017**, *9* (3), 2403–2409.

(68) Yang, X.; Wolcott, A.; Wang, G.; Sobo, A.; Fitzmorris, R. C.; Qian, F.; Zhang, J. Z.; Li, Y. Nitrogen-Doped ZnO Nanowire Arrays for Photoelectrochemical Water Splitting. *Nano Lett.* **2009**, *9* (6), 2331–2336.

(69) Hsu, Y. K.; Chen, Y. C.; Lin, Y. G. Novel ZnO/Fe_2O_3 Core–Shell Nanowires for Photoelectrochemical Water Splitting. *ACS Appl. Mater. Interfaces* **2015**, *7* (25), 14157–14162.

(70) Vuong, N. M.; Reynolds, J. L.; Conte, E.; Lee, Y. I. H:ZnO Nanorod-Based Photoanode Sensitized by CdS and Carbon Quantum Dots for Photoelectrochemical Water Splitting. *J. Phys. Chem. C* **2015**, *119* (43), 24323–24331.

(71) Cao, Y.; Dong, Y. J.; Chen, H. Y.; Kuang, D. B.; Su, C. CdS/CdSe Co-Sensitized Hierarchical TiO2 Nanofiber/ZnO Nanosheet Heterojunction Photoanode for Quantum Dot-Sensitized Solar Cells. *RSC Adv.* **2016**.

(72) Zhao, H.; Huang, F.; Hou, J.; Liu, Z.; Wu, Q.; Cao, H.; Jing, Q.; Peng, S.; Cao, G. Efficiency Enhancement of Quantum Dot Sensitized TiO_2/ZnO Nanorod Arrays Solar Cells by Plasmonic Ag Nanoparticles. *ACS Appl. Mater. Interfaces* **2016**, *8* (40), 26675–26682.

(73) Li, Z.; Yao, C.; Yu, Y.; Cai, Z.; Wang, X. Highly Efficient Capillary Photoelectrochemical Water Splitting Using Cellulose Nanofiber-Templated TiO_2

Photoanodes. *Adv. Mater.* **2014**, *26* (14), 2262–2267.

(74) Baek, M.; Kim, D.; Yong, K. Simple but Effective Way To Enhance Photoelectrochemical Solar-Water-Splitting Performance of ZnO Nanorod Arrays: Charge-Trapping Zn(OH) 2 Annihilation and Oxygen Vacancy Generation by Vacuum Annealing. *ACS Appl. Mater. Interfaces* **2017**, *9* (3), 2317–2325.

(75) Zhou, H.; Qu, Y.; Zeid, T.; Duan, X. Towards Highly Efficient Photocatalysts Using Semiconductor Nanoarchitectures. *Energy Environ. Sci.* **2012**, *5* (5), 6732.

(76) Grätzel, M. Photoelectrochemical Cells. *Nature* **2001**, *414* (6861), 338–344.

TOC Graphic

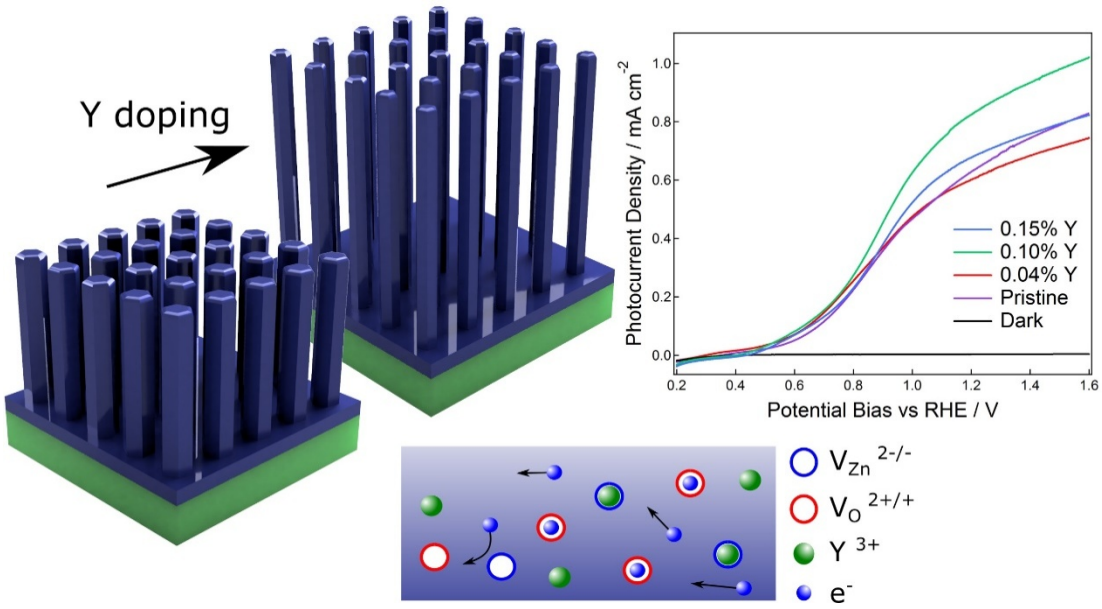
Y doping
Photocurrent Density / mA cm-2
Potential Bias vs RHE / V
0.15% Y
0.10% Y
0.04% Y
Pristine
Dark
VZn 2-/-
VO 2+/+
Y 3+
e-